PNAS RESEARCH ARTICLE | PHYSIOLOGY

A Na pump with reduced stoichiometry is up-regulated by brine shrimp in extreme salinities

Pablo Artigas[a,1], Dylan J. Meyer[a], Victoria C. Young[a], Kerri Spontarelli[a], Jessica Eastman[a], Evan Strandquist[b], Huan Rui[c], Benoît Roux[c], Matthew A. Birk[d], Hanayo Nakanishi[e], Kazuhiro Abe[e], and Craig Gatto[b]

Edited by Donald Hilgemann, Department of Physiology, The University of Texas Southwestern Medical Center, Dallas, TX; received August 14, 2023; accepted October 27, 2023

Brine shrimp (*Artemia*) are the only animals to thrive at sodium concentrations above 4 M. Salt excretion is powered by the Na^+,K^+-ATPase (NKA), a heterodimeric (αβ) pump that usually exports 3Na^+ in exchange for 2 K^+ per hydrolyzed ATP. *Artemia* express several NKA catalytic α-subunit subtypes. High-salinity adaptation increases abundance of $\alpha2_{KK}$, an isoform that contains two lysines (Lys308 and Lys758 in transmembrane segments TM4 and TM5, respectively) at positions where canonical NKAs have asparagines (*Xenopus* α1's Asn333 and Asn785). Using de novo transcriptome assembly and qPCR, we found that *Artemia* express two salinity-independent canonical α subunits ($\alpha1_{NN}$ and $\alpha3_{NN}$), as well as two β variants, in addition to the salinity-controlled $\alpha2_{KK}$. These β subunits permitted heterologous expression of the $\alpha2_{KK}$ pump and determination of its CryoEM structure in a closed, ion-free conformation, showing Lys758 residing within the ion-binding cavity. We used electrophysiology to characterize the function of $\alpha2_{KK}$ pumps and compared it to that of *Xenopus* α1 (and its $\alpha2_{KK}$-mimicking single- and double-lysine substitutions). The double substitution N333K/N785K confers $\alpha2_{KK}$-like characteristics to *Xenopus* α1, and mutant cycle analysis reveals energetic coupling between these two residues, illustrating how $\alpha2_{KK}$'s Lys308 helps to maintain high affinity for external K^+ when Lys758 occupies an ion-binding site. By measuring uptake under voltage clamp of the K^+-congener $^{86}Rb^+$, we prove that double-lysine-substituted pumps transport 2Na^+ and 1 K^+ per catalytic cycle. Our results show how the two lysines contribute to generate a pump with reduced stoichiometry allowing *Artemia* to maintain steeper Na^+ gradients in hypersaline environments.

electrochemical gradient | Na^+,K^+-ATPase | stoichiometry | extremophiles | transcriptome

Significance

Brine shrimp of the genus *Artemia* are the only animal that survives in saturated brine. High-salinity adapted *Artemia* were known to increase expression of a sodium pump subtype with two Asn-to-Lys substitutions compared to the ion-binding sites of canonical pumps. Here, we found that brine shrimp express two more salinity-independent sodium pumps and unequivocally demonstrate that the salinity-controlled, Lys-containing pumps exchange 2 $Na^+$for 1 K^+instead of the canonical 3$Na^+$for 2 K^+stoichiometry. This unique adaptation allows *Artemia* to build and maintain the larger Na^+electrochemical gradients imposed by their harsh environment.

Brine shrimp of the genus *Artemia* are crustaceans that adapt to salinities ranging from 20 mM NaCl to saturated salt solutions [i.e., up to 6 M salt, (1)]. These animals flourish in inland salt lakes, some of the harshest environmental conditions on earth, where brine-fly larvae are the only other animals known to persist. Brine shrimp are osmoregulators with a tightly regulated hemolymph (1, 2). The molecular mechanisms used by brine shrimp to tolerate the extremely high osmotic and ionic gradients are only partially understood (3). Some adaptive features include the presence of a hard integument and increased extrusion of Na^+ and Cl^- ions through specialized organs: the neck organ in the larval nauplii (4) and the metepipodites of the phyllopodia (flat thoracic appendages used for swimming) in adults (5).

A basolateral Na^+,K^+-ATPase (NKA) drives salt transport in ion-transport epithelia. The NKA is a heterodimeric P-type 2C ATPase formed by association of a catalytic α subunit (containing all the machinery for ion transport and ATP hydrolysis) and an auxiliary β subunit (essential for plasma membrane targeting) (6). Most animals have multiple NKA isoforms that form isozymes that operate with slightly different kinetic parameters (7), fine tuning the ion-transport needs of various cells (8). Canonical pumps export 3 Na^+ ions and import 2 K^+ per ATP molecule hydrolyzed (Fig. 1*A*) (9). It is thought that *Artemia* express two NKA α subunit isoforms (10): one isoform with canonical ion-binding sites ($\alpha1_{NN}$) and another with two striking asparagine-to-lysine substitutions within the ion-binding site region ($\alpha2_{KK}$, Fig. 1*B*), specifically, K308 in TM4 (equivalent to N333 in the canonical *Xenopus* α1) and K758 in TM5 (equivalent to N785) (11). Both isoforms are present in every salinity, but $\alpha2_{KK}$ mRNA expression increases drastically when brine shrimp are exposed to high salinity (12). It has been proposed that $\alpha2_{KK}$ may have a reduced ion stoichiometry helping *Artemia* adapt to high salinity by allowing it to build larger electrochemical gradients (12).

Here, we present a comprehensive study of the functional characteristics of *Artemia*'s $\alpha2_{KK}$ NKA and the cryoEM structure of $\alpha2_{KK}$ without transported ions, showing the presence of one of the two lysines within the ion-binding sites. To help interpret our results

Author contributions: P.A., D.J.M., H.R., B.R., M.A.B., K.A., and C.G. designed research; P.A., D.J.M., V.C.Y., K.S., J.E., E.S., H.R., M.A.B., H.N., K.A., and C.G. performed research; P.A., D.J.M., V.C.Y., K.S., J.E., E.S., H.R., M.A.B., K.A., and C.G. analyzed data; and P.A. wrote the paper.

The authors declare no competing interest.

This article is a PNAS Direct Submission.

[1]To whom correspondence may be addressed. Email: pablo.artigas@ttuhsc.edu.

This article contains supporting information online at https://www.pnas.org/lookup/suppl/doi:10.1073/pnas.2313999120/-/DCSupplemental.

Published December 11, 2023.

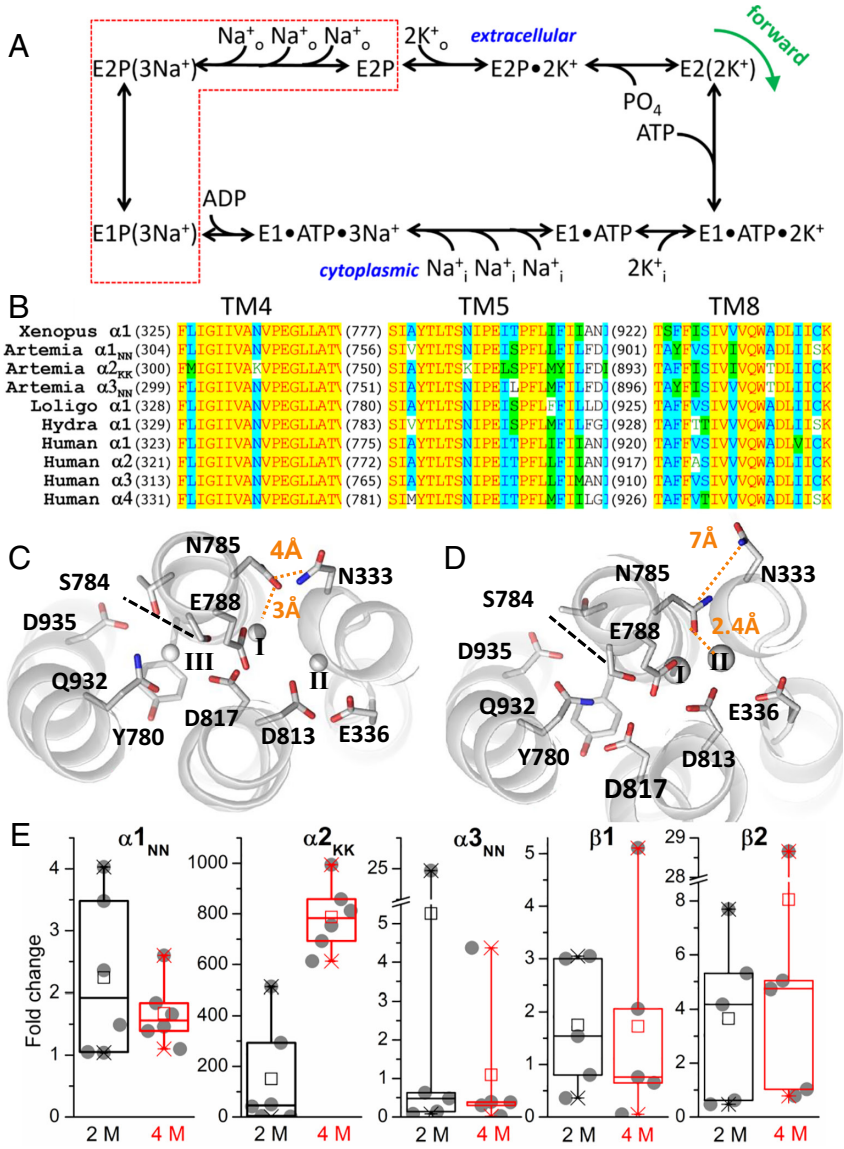

Fig. 1. (*A*) Post-Albers canonical Na^+, K^+-ATPase catalytic cycle. The pump transports one charge per cycle as it transports 3 Na^+ in exchange for 2 K^+ while harnessing the energy from ATP hydrolysis by alternating between phosphorylated and dephosphorylated forms of two major conformations E1 and E2. The red dotted box encloses the states transited by the pump in the absence of external K^+ in the presence of Na^+, when it produces the voltage-dependent transient charge movement. (*B*) Alignment of the TM4 and TM5 regions of various NKA α subunits showing the two lysines present in *Artemia*'s $\alpha2_{KK}$ (third line), where canonical NKAs have asparagines. (*C* and *D*) Extracellular view of the ion-binding site region showing ion-coordinating sidechains and N333 (*Xenopus* α1 numbering) in the structures of the pig NKA formed by α1β1γ, with 3 Na^+ ions bound in E1 (13) (*C*) and of the shark NKA formed by α1β1FXYD10 with bound K^+ in E2 (14) (*D*). (*E*) Box plot of fold-change of *Artemia*'s NKA isoforms in adult shrimp at high salinities. Data points from 5 ($\alpha3_{NN}$, β1 & β2) or 6 ($\alpha1_{NN}$ & $\alpha2_{KK}$) biological replicates are shown as circles. The box edges are the quartiles, the line dividing the box is the median, the mean is an open square. A Kruskal–Wallis test indicates that only $\alpha1_{NN}$ at 2 M ($P = 0.006$) and 4 M ($P = 0.01$) and $\alpha2_{KK}$ ($P = 0.0001$) at 4 M, are ≠ than 1 (no change).

in structural terms, we utilized molecular dynamics (MD) simulations performing in silico mutagenesis on previously available ion-bound X-ray structures of canonical NKAs, which further suggest how the double lysine substitution may reduce stoichiometry and significantly alter ion-binding reactions. We utilized two-electrode voltage clamp (TEVC) and patch-clamp electrophysiology in *Xenopus* oocytes to characterize the function of $\alpha2_{KK}$ pumps and compared it to the function of canonical NKA and its double-lysine substituted mutant that mimics *Artemia*'s $\alpha2_{KK}$. We show that introduction of the two lysines on a canonical NKA background recapitulates the functional characteristics of *Artemia*'s $\alpha2_{KK}$ with respect to external ion interaction. Due to limited expression of $\alpha2_{KK}$ pumps, we measured ^{86}Rb uptake under voltage clamp in the double-lysine substituted *Xenopus* α1 and demonstrate that it transports 2 Na^+:1 K^+ per cycle instead of the 3 Na^+:2 K^+ observed in canonical NKAs, thus allowing $\alpha2_{KK}$ pumps to build larger electrochemical gradients. By comparing the functional consequences of single- and double-lysine substitutions, we show how the interaction between both residues may be needed to maintain physiologically relevant affinities for Na^+ and K^+ that ensure $\alpha2_{KK}$ NKAs are functional under *Artemia*'s natural environmental conditions. Thus, our results demonstrate experimentally how both evolutionarily substituted lysine residues are required for the reduced stoichiometry of $\alpha2_{KK}$ to confer an advantage to brine shrimp, allowing them to generate a larger gradient across the membranes expressing these NKAs.

Results

Our initial attempts to express the published version of *Artemia*'s $\alpha2_{KK}$ (11) and β (15) in *Xenopus* oocytes were unsuccessful. Therefore, we raised *Artemia* at three salinities, 250 mM, 2 M,

and 4 M salt (mostly NaCl, see *Methods*), to perform RNAseq and de novo transcriptome assembly. The resulting transcriptome contains two β subunit splice variants (β1 and β2). While β1 differs from previously available sequences at a few residues within the extracellular globular domain (15), β2 has a distinct N terminus (*SI Appendix*, Fig. S1). We also found three, instead of two, catalytic subunit isoforms: $\alpha1_{NN}$, $\alpha2_{KK}$, and $\alpha3_{NN}$ (*SI Appendix*, Fig. S2). The $\alpha1_{NN}$ sequence has a longer N terminus than a previously reported sequence (16), while $\alpha3_{NN}$, the isoform with the lowest transcript abundance, also has canonical sites. The noncanonical $\alpha2_{KK}$ from our RNAseq is almost identical to the originally described sequence (P17326, ref. 11), except for three residues in the intracellular loop between TM6 and TM7. All α and β isoform sequences are found in the recently published genome (17).

The aligned sequences of the ion-binding site regions of α subunits from *Artemia* and other species illustrate the unique lysine substitutions residing in TM4 and TM5 of $\alpha2_{KK}$, where canonical α subunits have asparagine residues (Fig. 1*B*). The zoomed-in structural view of the ion-binding sites in the 3 Na^+-bound [Fig. 1*B*, (13)] and 2 K^+-bound [Fig. 1*C*, (14)] states show that N785 in TM5 (*Xenopus* α1 numbering) directly coordinates bound ions, while N333 in TM4 is further away. We used qPCR to interrogate which NKA isoforms change expression at different salinities (*Methods*). Consistent with previous reports that considered an incomplete set of isoforms (12), we found that $\alpha2_{KK}$ is drastically up-regulated when *Artemia* shrimp adapt to high salinity, while changes in the other four isoforms are minor (Fig. 1*D*). Compared to 250 mM salt, the increase in $\alpha2_{KK}$ mRNA at 2 M salt was highly variable (150 ± 208-fold, SD), but a much higher expression was always observed at 4 M salt (787 ± 133 fold increase, SD).

We expressed the noncanonical $\alpha2_{KK}$ (P17326, see *Methods*) in HEK cells for structural studies (Fig. 2) and in *Xenopus* oocytes for functional evaluation (Fig. 3). NKA-mediated currents (measured in 125 mM Na^+ with 10 mM K^+) were larger in oocytes injected with $\alpha2_{KK}$ and β2 (51 ± 19 nA, $n = 48$) compared to those injected with $\alpha2_{KK}$ and β1 (31 ± 16 nA, $n = 9$), but substantially smaller than currents mediated by *Xenopus* α1β3 in the same conditions (330 ± 186 nA, $n = 49$) or by previously reported NKA isoforms from several species (18–22). Given the higher expression with β2 versus β1, the β2 isoform was used as the partner for expression of *Artemia*'s α2 in all further studies.

Protein expressed in HEK cells was purified in the absence of transported ions, and the ion-free $\alpha2_{KK}$β2 structure in the presence of the inhibitor AlF_4^- was determined to 3.4 Å resolution by cryoelectron microscopy (*SI Appendix*, Fig. S3 and Table S3). The overall structure shows an E2 arrangement (Fig. 2), viewed from the membrane plane in Fig. 2*A*. The arrangement of the transmembrane helices is close to that observed in the pig NKA with 2 K^+ ions occluded E2-P state (2zxe), with a RMSD of 1.43 Å (*SI Appendix*, Fig. S4). The density map (Fig. 2 *B* and *C*) shows the TGES-motif of the A domain interacting with the AlF_4^- bound to the P-domain (Fig. 2*C*), a hallmark of the E2-P state. The zoomed-in slice shows that the ion-binding region is inaccessible to the extracellular solution (*SI Appendix*, Fig. S5). Thus, despite the absence of transporting cations in this experimental set-up, the $\alpha2_{KK}$β2 molecule accumulates in an E2-P occluded-like state.

Many side chains around the ion-binding region are well defined, including the noncanonical lysines: Lys308 (corresponding to *Xenopus* α1 Asn333) and Lys758 (*Xenopus* α1 Asn785) (Fig. 2*B*). The amino group of Lys308 is within hydrogen-bond distance of the main-chain oxygen of Met275 in TM3, facing away from the binding cavity (Fig. 2*C*). In contrast, the side chain of Lys758 in TM5, occupies the space between cation-binding

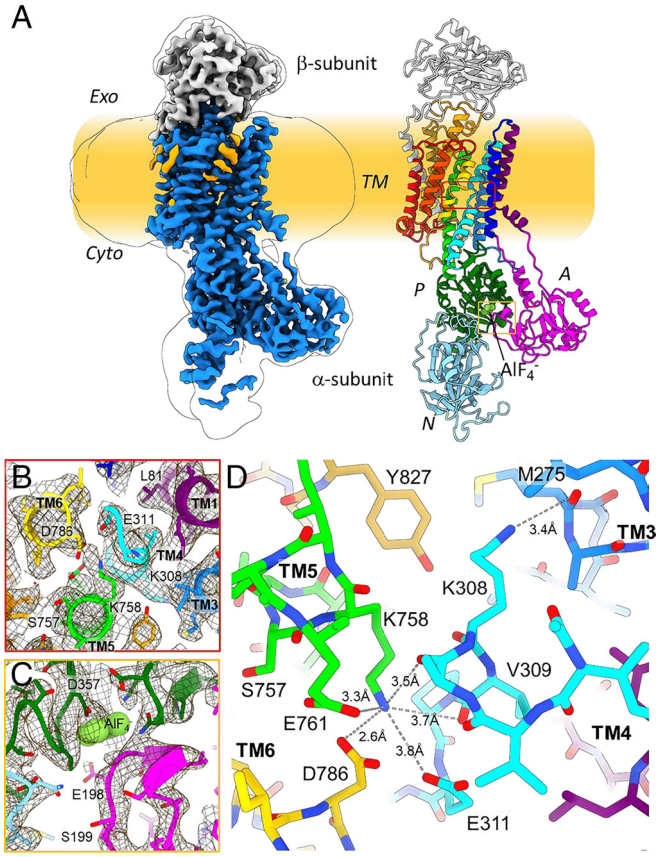

Fig. 2. Structure of *Artemia*'s $\alpha2_{KK}$β2. (*A*) Overall cryo-EM structure of *Artemia's* $\alpha2_{KK}$ in the AlF_4 inhibited E2 state without bound ions viewed from the membrane plane showing the α (multicolored) and β subunits (yellow). Intracellular A-, P-, and N-domains are colored pink, green, and cyan. The membrane position is indicated by the yellow shade. (*B* and *C*) Density map in the region surrounding the ion-binding sites (*B*) and in the P domain, where AlF_4^- binds to the P-type ATPase conserved aspartic acid (*C*). (*D*) Zoomed-in view of the ion binding site region of the $\alpha2_{KK}$ structure viewed from the extracellular side, approximately perpendicular to the membrane plane, a similar orientation as the ion-bound canonical structures shown in Fig. 1*C*.

sites I and II with its ε-amino group likely forming a salt-bridge with TM6's Asp786 (*Xenopus* α1 Asp813, Fig. 2*C* and *SI Appendix*, Fig. S4 *B* and *C*). Other potential electron donors in close proximity include the main chain carbonyls from Ala307 and Val309 in TM4 and the side chain carboxyl groups from Glu311 in TM4 (E336 in *Xenopus*) and Glu761 in TM5 (E788 in *Xenopus*). These amino acids primarily coordinate K^+ at site II in the canonical 2 K^+-occluded E2-P state (*SI Appendix*, Fig. S4 *B* and *C*). Thus, in the absence of transported cations, Lys758 appears to interact mostly with what corresponds to site II in the canonical NKAs, leaving an empty space (presumably occupied by water) surrounded by the site I-coordinating residues Ser757, Glu761, and Asp790 (*SI Appendix*, Fig. S5, *Xenopus* S784, E788, and D817). Because this empty space is too small to simultaneously accommodate two K^+ ions, our structure suggests that the charged sidechain of Lys758 might substitute for one transported ion. However, the structure alone falls short of demonstrating a noncanonical NKA stoichiometry, or how the lysine residues might interact to maintain a functional NKA under physiological conditions.

To further evaluate the structural distortion within the membrane region, we introduced the lysine mutations in silico within available structures of canonical α1 NKAs with 3 Na^+-bound in E1 (13) and with 2 K^+-bound E2 (14) and performed molecular dynamics (MD) simulations. We used the simulation trajectories

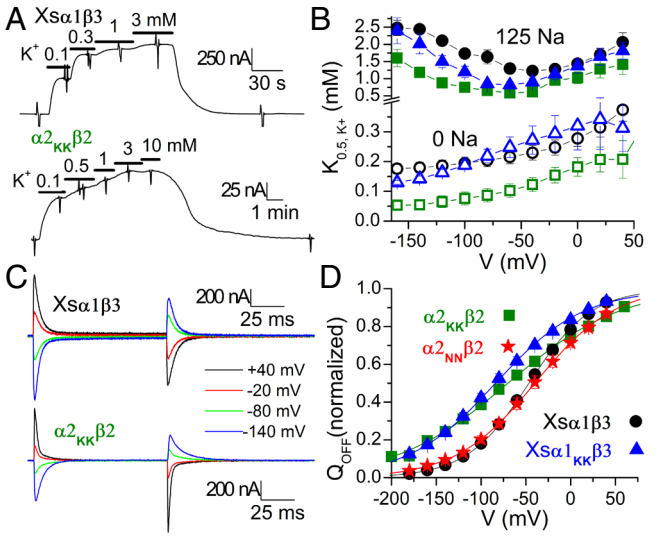

Fig. 3. Electrophysiological characterization of *Artemia*'s $\alpha2_{KK}\beta2$ NKAs. (*A*) Representative traces in NMG^+ solution at −50 mV, from oocytes injected with cRNA to form *Xenopus* α1β3 (*Top*) or *Artemia*'s $\alpha2_{KK}\beta2$ (*Bottom*) NKAs. Addition of K^+ activated outward currents in a concentration-dependent manner. Vertical deflections in the traces correspond to application of 100 ms-long voltage pulses used to obtain the K^+-induced currents at different voltages to measure the half-maximal activating concentration. (*B*) $K_{0.5,K}$ obtained from Hill fits to the K^+ concentration dependence of the steady-state current, as a function of the applied voltage obtained in the presence (solid symbols) or absence of Na^+ (as in *A*, open symbols) for oocytes expressing *Xenopus* α1β3 (black circles) *Artemia*'s $\alpha2_{KK}\beta2$ (green squares) or the double lysine mutant mimicking $\alpha2_{KK}$, *Xenopus* $\alpha1_{KK}\beta3$ (blue triangles). The Hill fits had Hill coefficient (shared between all voltages) were n_H = 1.20 ± 0.09 for Xsα1β3, n_H = 1 (fixed) for $\alpha2_{KK}\beta2$ and n_H =1.06 ± 0.08 for Xsα1KKβ3 in NMG, and n_H = 1.55 ± 0.09 (n = 13) for Xsα1β3, n_H = 1 (fixed) for $\alpha2_{KK}\beta2$ and n_H = 0.86 ± 0.09 (n = 5) for $Xs\alpha1_{KK}\beta3$. (*C*) Ouabain-sensitive transient currents (current without ouabain – current after ouabain) measured in the presence of 125 mM Na^+ when voltage pulses were applied from −50 mV to the indicated voltages, in two oocytes expressing *Xenopus* α1β3 (*Top*) or *Artemia*'s $\alpha2_{KK}\beta2$ (*Bottom*). (*D*) Q-V curve plotting the integral of the current signal when the voltage pulse is turned off as a function of the applied voltage for the same constructs in *B*. Line plots correspond to Boltzmann equations fitted to the data from individual experiments (*Methods*) with slope factors shared between all Boltzmann fits to different experiments (±SEM from global fit) kT/ze_q = 35 ± 0.3 mV (n = 18) for Xsα1β3, kT/ze_q = 64 ± 2.3 mV (n = 9) for $\alpha2_{KK}\beta2$; kT/ze_q = 49 ± 1.3 mV (n = 7) for $Xs\alpha1_{KK}\beta3$, and kT/ze_q = 44 ± 2.6 mV (n = 5) for $\alpha2_{NN}\beta2$ and the midpoint voltage given in Table 1. The IC_{50} for inhibition of $\alpha2_{KK}$-mediated K^+-induced currents by the specific inhibitor ouabain was 135 ± 90 μM (SD, n = 14) thus allowing separation of exogenous from endogenous currents by preincubation in 1 μM ouabain (*Methods*).

to measure the RMSD of the ion-binding sites (Table 1), distinguishing effects on the bound ions (RMSD, ions) and the nonhydrogen atoms of the ion-binding-site residues (RMSD, residues). The systems for $\alpha1_{K785}$ and $\alpha1_{K333/K785}$ became particularly unstable for K^+ ions in E2, due to the $-NH_3^+$ sidechain group of K785 acting as a cation surrogate. Consistent with this proposal, removing one bound ion from one site of the $\alpha1_{K333/K785}$ simulations restored ion-binding-site stability for both, Na^+ in E1 and K^+ in E2 (Table 1). Representative snapshots from one replica in each system during MD simulations are shown in *SI Appendix*, Fig. S6.

Functional implications of structural alterations were evaluated by comparing the electrophysiological parameters of $a2_{KK}\beta2$ to canonical pumps. Net transport of one charge in each cycle generates an outward current when the oocyte is exposed to extracellular K^+ in the presence of intracellular Na^+. Representative traces from Na^+-loaded oocytes at −50 mV, bathed by external N-methyl D-glucamine (NMG^+), illustrate outward currents induced by step changes in K^+ concentration in oocytes expressing canonical *Xenopus* α1β3 pumps (Fig. 3 *A*, *Top*), or *Artemia*'s $\alpha2_{KK}\beta2$ (Fig. 3 *A*, *Bottom*). Vertical deflections correspond to 100 ms-long step changes in voltage to measure the K^+-activated currents at different voltages, to obtain the half-maximal activating concentration ($K_{0.5,\ K}$) as a function of voltage (Fig. 3*B* and Table 1). The $K_{0.5,K}$ was measured in the presence (solid symbols) and absence (open symbols) of external Na^+. The presence of Na^+ increases $K_{0.5,K}$ at all voltages due to Na^+ and K^+ competition, but the increase is larger at negative voltages due to the stronger voltage dependence of external Na^+ binding (24). *Xenopus* α1β3 (Xsα1β3, black circles) and *Artemia*'s $\alpha2_{KK}\beta2$ pumps (green squares) have similar apparent affinities for K^+. We mutated Asn333 and Asn785 to lysine in the *Xenopus* α1 subunit, to mimic $\alpha2_{KK}$. K^+-activated NKA currents of oocytes injected with the double-lysine mutant and β3 ($Xs\alpha1_{KK}\beta3$) have similar characteristics to those in $\alpha2_{KK}$, including reduced 10 mM K^+-induced current amplitude in 125 mM Na^+ (169 ± 147 nA, n = 15,) and affinities for external K^+ like those of $\alpha2_{KK}$ and the canonical *Xenopus* wild type (Fig. 3*B*, blue triangles). The curve for $\alpha2_{KK}$ appears slightly left shifted with respect to *Xenopus* α1β3, while the curve of $\alpha1_{KK}\beta3$ falls between the curves of *Artemia* $\alpha2_{KK}$ and wild-type *Xenopus* α1 (Fig. 3*B*). The apparent affinity for external K^+ without Na^+ of noncanonical pumps is increased twofold with respect to the *Xenopus* constructs. Thus, the small voltage-dependent differences observed in the presence of external Na^+ probably reflect the slightly higher apparent affinity for external K^+ of noncanonical pumps and the lower apparent affinity for external Na^+ of both the lysine-containing pumps.

Voltage-dependent transient-charge movement in the absence of external K^+ allows evaluation of enzyme interaction with extracellular Na^+. Square-voltage pulses from −50 mV to voltages ranging from −180 to + 40 mV were repeated, first in the absence, and then in the presence of an NKA inhibitor (1 mM ouabain), to obtain the ouabain-sensitive transient currents (Fig. 3*C*). Integration of the current observed when the voltage returns to −50 mV yields the charge moved, which is plotted against the voltage of the preceding pulse in the Q-V curve (Fig. 3*D*). The sigmoidal Q-V curves are described by a fit to a Boltzmann equation (line plots). Compared to the canonical *Xenopus* α1 (black circles), the curve for *Artemia* $\alpha2_{KK}\beta2$ (green squares) is shallower (larger slope factor, see *Methods*) and the center shifted to more negative voltages. The charge movement of the *Xenopus* $\alpha1_{KK}$ mutant is also left-shifted compared to the wild-type α1 (Fig. 3*D* and Table 1) and has a smaller increase in the slope factor. The reciprocal substitution making a canonical NKA in the brine shrimp's $\alpha2_{KK}$ background by replacing the lysines with asparagines moved the Q-V curve to the right and increased the slope (Fig. 3*D*, red stars). While slope factor changes are difficult to interpret (25), the center of the Boltzmann distribution, $V_{1/2}$, relates to the overall apparent affinity for external Na^+. A left-shifted curve indicates a reduced Na^+ affinity, whereas a right-shifted curve suggests an increased affinity for Na^+ (25 mV shift per twofold change in affinity) (26, 27). Thus, compared to *Xenopus* α1, *Artemia* $\alpha2_{KK}$ and the *Xenopus* $\alpha1_{KK}$ mutant have a ~threefold reduction in apparent affinity for external Na^+.

Attempts to reliably measure ATP-activated currents in *Artemia* $\alpha2_{KK}$ in giant patches were unsuccessful as the currents were too small for reliable reproducible measurement. Thus, we utilized giant inside-out patches from oocytes expressing wildtype or double lysine-substituted *Xenopus* α1 with saturating external K^+ in the pipette's extracellular solution. ATP-induced NKA currents were measured in the presence of variable intracellular Na^+ without intracellular K^+ (Fig. 4*A*) and plotted as a function of intracellular Na^+ concentration (Fig. 4*B*). Each individual experiment was fitted with the Hill equation yielding average $K_{0.5}$ values in Table 1. The double lysine mutation reduced intracellular Na^+ apparent affinity to a similar extent as external Na^+ affinity (threefold).

Table. 1. Average RMSD of binding-site residues and ions from MD simulations of the ion-bound E1 and E2 states (left 4 columns) and functional parameters (right three columns) from TEVC ($K_{0.5,K}$ and $V_{1/2}$) and patch clamp ($K_{0.5,Na}$) experiments

	RMSD, residues		RMSD, ions		Functional parameters		
	E1	E2	Na^+ in E1	K^+ in E2	$K_{0.5,K}$ (mM)	$V_{1/2}$ (mV)	$K_{0.5,Na}$ (mM)
Canonical α1	1.39 ± 0.09	0.82 ± 0.03	2.43 ± 0.09	0.73 ± 0.11	0.21 ± 0.10 (*n* = 19)	−47 ± 7 (*n* = 18)	3.3 ± 0.25 (*n* = 3)
$\alpha1_{K333}$	**2.01 ± 0.14**	1.10 ± 0.28	2.39 ± 1.11	1.06 ± 0.39	0.12 ± 0.06 (*n* = 5)	**−117 ± 23** (*n* = 18)	**6.4 ± 0.1** (*n* = 3)
$\alpha1_{K785}$	1.75 ± 0.17	**2.26 ± 0.42**	1.95 ± 0.12	**3.21 ± 0.83**	**2.66 ±2.08** (*n* = 8)	**−120 ± 11** (*n* = 8)	**9.3 ± 0.4** (*n* = 3)
$\alpha1_{KK}$	**1.93 ± 0.03**	1.83 ± 0.38	**3.50 ± 0.21**	**19.5 ± 28.2**	0.25 ± 0.09 (*n* = 7)	**−84 ± 8** (*n* = 7)	**10.2 ± 2.1** (*n* = 3)
$\alpha1_{KK}$ −1 cation	1.61 ± 0.07	1.35 ± 0.07	1.72 ± 0.13	1.84 ± 0.08			
$\alpha2_{KK}$	ND	ND	ND	ND	0.10 ± 0.06 (*n* = 6)	−70 ± 12 (*n* = 9)	ND
$\alpha2_{NN}$	ND	ND	ND	ND	ND	−40 ± 12 (*n* = 5)	ND

For MD simulations, residues within 4.5 Å to any of the bound ions were assigned as binding-site residues. Errors are SEM calculated from three replicas. When the site II ion was removed from N333K/N785K the E1 system was unstable. The wild-type simulation RMSD are from ref. 23. For functional experimental parameters, errors are SD. The Hill coefficients for K^+ interaction with $\alpha1_{K333}$ and $\alpha1_{K785}$ were n_H = 1.28 ± 0.07 and n_H = 1.14 ± 0.08, respectively. And for intracellular Na^+ n_H = 2.5 ± 0.69 and n_H = 1.3 ± 0.69. The slope factors from Q-V curves were kT/ez_q = 52 ± 2 mV (*n* = 13) for $\alpha1_{K333}$ and kT/ez_q = 45 ± 2 mV for $\alpha1_{K785}$. Quantities in bold font illustrate large deviations from wild-type canonical parameters.

The stoichiometry of the double lysine mutant was determined by measuring the uptake of radioactive $^{86}Rb^+$ [a K^+ congener with affinity similar to K^+ (28) in oocytes under two-electrode voltage clamp (Fig. 4*C*). The current traces at −50 mV show that perfusion of 1 mM $^{86}Rb^+$ in the NMG^+ solution evoked outward pump current in oocytes injected with both wild-type *Xenopus* α1β3 (Fig. 4 *C*, *Top*) or the *Xenopus* $\alpha1_{KK}\beta3$ mutant (Fig. 4 *C*, *Bottom*). After 2–3 min, the $^{86}Rb^+$ was washed away and the current returned to baseline. The oocyte was collected and the indicated level of $^{86}Rb^+$ uptake by the oocyte was determined. The integral of I_P gives the charge extruded by the oocyte (converted to moles of elementary charge using Faraday's constant). The mean ratio of imported Rb^+/exported charge in individual oocytes was 2.11 ± 0.46 (*n* = 40, SD) for wild type and 1.06 ± 0.20 (*n* = 21, SD) for $\alpha1_{KK}$ (Fig. 4*D*). This result demonstrates that 3 Na^+ are exported for 2 Rb^+ imported in wild-type canonical pumps, as expected, while pumps with the two lysine residues export 2 Na^+ per Rb^+ imported.

The functional characteristics of the single mutants were also evaluated (Table 1), completing the mutant cycle to determine whether the two residues are energetically coupled. Compared to wild type ($K_{0.5}$ = 0.21± 0.10), the affinity for external K^+ was reduced by ~20-fold in the $\alpha1_{K785}$ mutant ($K_{0.5}$ = 2.66 ± 2.08), while $\alpha1_{K333}$ ($K_{0.5}$ = 0.12 ± 0.06) resembles wild type. Both single lysine mutants $\alpha1_{K333}$ and $\alpha1_{K785}$ caused an ~eightfold reduction in apparent affinity for external Na^+ (~−75 mV shift to the left in Q-V curve). The apparent affinity of intracellular Na^+ was 3.3 ± 0.25 (*n* = 3) for wild type 6.4 ± 0.1 (*n* = 3) for $\alpha1_{K333}$ (twofold reduction in affinity) and 9.3 ± 0.4 (*n* = 3) for $\alpha1_{K785}$ (threefold reduction in affinity). Thus, mutant cycle analysis demonstrates energetic coupling between the two mutations, as the effect of the double mutant on the $K_{0.5}$ for K^+ and Na^+ is different than the additive effects of each single mutation. This interaction is likely critical for this pump to function under physiological conditions.

Discussion

Since determination of the first P-type ATPase structures, it has been suspected that certain NKA isoforms with cationic amino acids in their ion-binding sites may have an altered stoichiometry. Given that expression of these NKA isoforms increases when osmo-regulating animals adapt to extreme salinities, it suggests that this characteristic may allow them to maintain larger electrochemical gradients. Our results demonstrate the noncanonical stoichiometry of provide the high-resolution structure of an environmentally regulated NKA.

Structural Features of $\alpha2_{KK}$ Pumps. Our $\alpha2_{KK}\beta2$ structure shows that the amino group of Lys758 points to site II rather than site I. H,K-ATPases (HKA) have a lysine residue at the contiguous position, equivalent to Ser784 in NKA. The proximity of position 784 to site I ensures that site I is physically blocked by the lysine in HKA, ensuring a single K^+ binds to site II, contrasting with our observations with K758 in $\alpha2_{KK}$.There are two possibilities for a single K^+ ion binding in $a2_{KK}$: 1) K^+ might bind to site I, electrostatically repulsing Lys758's ε-amino group toward the unwound part of TM4 and improving its interaction with the site II amino acids to trigger dephosphorylation, or 2) the ε-amino group of Lys758 may orient toward site I and the K^+ ion is occluded in site II. The first hypothesis appears structurally more feasible because in canonical NKAs K^+ at site II is coordinated by three main-chain and one side-chain oxygen atoms from TM4's unwound region, which are found at distances (2.8 Å–3.2 Å, 2zxe) that would be ideal for hydrogen bonds to form between nitrogen and oxygen, and we observe similar distances between the ε-amine of Lys758 and the surrounding oxygens in the *Artemia* $a2_{KK}$ structure (Fig. 2*D* and *SI Appendix*, Figs. S4 and S7*A*). The second hypothesis appears less likely because the ε-amine and δ-carbon of Lys758 would clash with site II even if the Lys758 side chain faces site I (*SI Appendix*, Fig. S7*B*). An ion-bound structure is needed to unequivocally distinguish between these possibilities.

Lys308, the other lysine in $\alpha2_{KK}\beta2$, interacts with the main chain carbonyl of Met275 in TM3, a residue that corresponds to an asparagine in canonical NKAs (Asn333 in *Xenopus* α1) and to a tyrosine (Tyr340) in the gastric HKA. The mutation Tyr340Asn is one of five simultaneous substitutions required to engineer a second K^+-binding site in the gastric HKA (29). It is thought that this substitution alters the rotamer of Asn792 (which corresponds to Lys758 $\alpha2_{KK}$) by interacting with Tyr863 (Tyr854 in canonical NKAs and Tyr827 in $\alpha2_{KK}$). We therefore speculate that Lys308 in $\alpha2_{KK}\beta2$ indirectly adjusts the position of Lys748 helping them

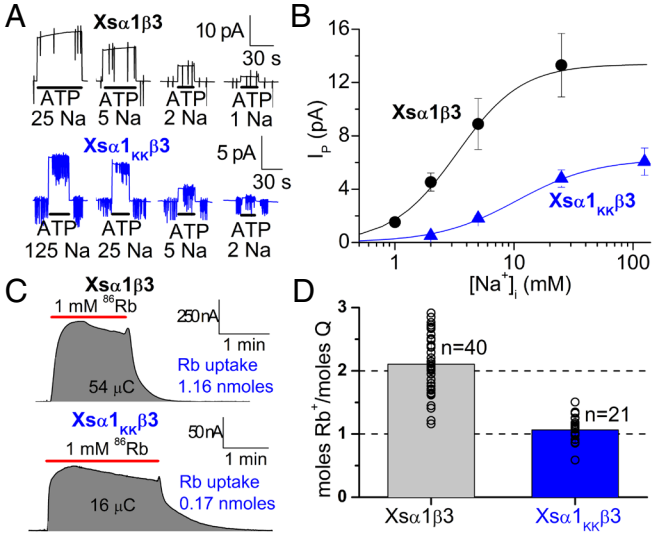

Fig. 4. Intracellular Na^+ affinity and stoichiometry of $\alpha1_{KK}\beta3$. (*A*) Representative traces from two patches held at 0 mV. Application of 4 mM MgATP at different intracellular Na^+ concentrations induced larger outward NKA currents as Na^+ concentration is raised. Sharp vertical deflections correspond to application of 25 ms pulses ranging from −140 to +40 mV. (*B*) Average NKA current as a function of Na^+ from three patches for each mutant. Line plots represent the Hill equations with parameters $K_{0.5,Na}$ = 3.3 ± 0.25, n_H = 1.6 ± 0.1 for wild-type Xsα1β3 (black circles) and $K_{0.5,Na}$ =10.2 ± 2.1 n_H =1.3 ± 0.1 (black circles) for $Xs\alpha1_{KK}\beta3$ (blue triangles). The three individual experiments were fitted with a shared Hill coefficient. Error bars are SEM from the fit. (*C*) Representative traces from oocytes expressing wild-type Xsα1β3 (*Top*) or $Xs\alpha1_{KK}\beta3$ (*Bottom*), held at −50 mV bathed by NMG. Application of 1 mM $^{86}Rb^+$ over the oocytes reversibly induced outward current. The current integral gives the charge extruded by the oocytes. After current deactivation, the total $^{86}Rb^+$ uptake by each oocyte was measured in a scintillation counter, indicated for individual experiments. (*D*) Bar graph summarizing the average ratio of Rb^+ uptake/charge extruded from the indicated number of oocytes (from two oocyte batches for each mutant). The total uptake was 1.00 ± 0.06 nanomoles in oocytes expressing WT pumps, 465 ± 39 picomoles, 283 ± 54 picomoles in oocytes expressing N333K/N785K, and 17 ± 4 picomoles (n = 12) in impaled uninjected oocytes pretreated with ouabain. Non-NKA-mediated uptake (i.e., uptake in uninjected oocytes) was subtracted from the uptake measured in injected oocytes in the same batch of oocytes to obtain the NKA-mediated uptake (*Methods*).

occupy one of the two binding sites when the pump is open to the external side, a hypothesis supported by functional studies discussed below.

Although we lack an E1 structure, all residues required to form Na^+ site III are present in $\alpha2_{KK}$ with identical side chain arrangements as in canonical NKA E2 structures (*SI Appendix*, Fig. S4). These residues include those that directly coordinate Na^+ (Tyr753, Asp906, and Q903) (27, 30–32) and those indirectly contributing to site III formation (Cys907, Trp904, and Glu934), some of which are absent in HKA pumps (33, 34). Importantly, a lysine at the position equivalent to *Xenopus* N785 maintains the selectivity for cytosolic Na^+ (Fig. 4), while the presence of a lysine at the contiguous position in HKAs (*Xenopus* 784) is required for proton selectivity (29, 33). Interestingly, Ser784Lys, eliminates $^{86}Rb^+$ uptake in NKA (35), indicating that the continuous occupancy of site I by Lys784 side chain blocks NKA function, probably by steric hindrance of access to site III, the first site to bind Na^+. In the canonical binding sequence, Na^+ binding to site III forms site I, subsequent Na^+ binding to site I forms site II, and Na^+ binding to site II triggers full Na^+-occlusion and phosphorylation (13). Considering the electrogenicity of $\alpha2_{KK}\beta2$ and the 2 Na^+:1 K^+ stoichiometry measured in $\alpha1_{KK}\beta3$ (the $\alpha2_{KK}$ mimic), two Na^+ ions must bind in the inward-facing E1 state, meaning that Lys758 between sites I and II, must occupy sufficient space to ensure that only Na^+ reaches site III to initiate the occlusion sequence with high selectivity. Such a mechanism would be consistent with a recent proposal, in which Mg^{2+} binds to E1 between site I and site II, leaving room for a Na^+ to enter site I to initiate occlusion (36). Thus, we propose that after site III occlusion, the ε-amino group will move to site I, followed by binding of Na^+ at site II, triggering final occlusion and phosphorylation. Another unlikely alternative, due to conservation of site II as the main transport site in P-type ATPases, is that the lysine occupies site II, meaning site I is the last to bind before complete occlusion of two Na^+ ions in this pump. The concrete resolution between these two alternatives will require solving the 2 Na^+-bound E1 structure of $\alpha2_{KK}$ pumps.

Functional Characteristics of Pumps with Noncanonical Lysine Residues at TM4 and TM5. Structural and MD studies conducted here suggest that pumps with a lysine at positions 333 and 785, where the *Xenopus* α1 and other canonical pumps have asparagines, should have altered stoichiometry. Our ^{86}Rb uptake experiments demonstrate such reduced stoichiometry that, as discussed below, likely contributes to *Artemia's* ability to adapt to higher salinities. The effect on external Na^+ interaction of the double lysine substitution on canonical NKAs is of similar amplitude and in opposite direction to the substitution of the two $\alpha2_{KK}$ lysines with asparagines. The presence of the two lysines yields NKAs with reduced expression, that appear less stable than canonical NKAs. Examination of our structure indicates that K758, the lysine in TM5, is necessary to occupy one binding site, substituting for one K^+ in E2 and one Na^+ in E1. We infer the importance of TM4's K308 in $\alpha2_{KK}$ from our mutant cycle analysis.

Individual lysines introduced at the equivalent positions of canonical NKAs had distinct effects on ion binding (Table 1). Compared to the canonical template, N785K reduced apparent affinity for both Na^+ and K^+, a result consistent with the removal of the oxygen coordinating both K^+ ions bound in E2 and one of the Na^+ ions bound in E1 of canonical NKAs (Fig. 1*C*). However, N333K reduced apparent affinity for Na^+ without modifying the apparent affinity for K^+. This observation is consistent with previously published structures of canonical NKAs which show a hydrogen bond between N333 and N785 in Na^+-bound E1; this hydrogen bond is absent in the K^+-bound E2 structure where N333 points away from the binding sites, as seen in our $\alpha2_{KK}$ structure. The simultaneous lysine substitutions caused nonadditive effects that demonstrate energetic coupling between these residues. Substitution of N333K on the N785K background increases apparent affinity for external Na^+ and K^+ compared to the N785K mutant. This suggests that the lysine in TM4 helps rescue the K^+-affinity of the lysine in TM5. With respect to intracellular Na^+ binding, the $K_{0.5}$ for intracellular Na^+ of the double mutant measured in patch clamp experiments (Fig. 4) is similar to that of single mutants (Table 1). Therefore, based on the shift observed in Q-V curves (Table 1), the double mutant has a higher extracellular Na^+ affinity (i.e., smaller $K_{0.5}$) than either single mutant, but it does not alter intracellular Na^+ affinity, indicating that the lysine alters the external and internal occlusion rates to different extents.

We measured the apparent, rather than the real, affinity for intracellular Na^+ (which is affected by the occupancy of all states in the cycle). Jorgensen and Amat (12) studied the effect of the two lysine substitutions on Na^+-dependent phosphorylation of pig α1β1 pumps in the presence of oligomycin to evaluate affinity for intracellular Na^+. They observed ~10-fold reductions in affinity for intracellular Na^+ binding in all mutants (the two single mutants and the double lysine mutant). Thus, while the presence of a lysine in TM4 ensures that the high affinity for extracellular K^+ is

maintained, we have yet to confirm the affinity of *Artemia*'s pumps for intracellular Na^+. Based on transient charge movement in our $\alpha2_{KK}$ and $\alpha2_{KK}$-mimic pumps, as well as in measurements of intracellular Na^+ affinity in the $\alpha1_{KK}$ mimic, $\alpha2_{KK}$ appears to have a slightly lower apparent affinity for intracellular Na^+ than most canonical NKAs. Speculatively, this reduced affinity for intracellular Na^+ may serve as a reservoir for sodium pumping capacity under conditions of elevated intracellular Na^+. Specifically, rising intracellular Na^+ in salt gland cells may be the signal to increase $\alpha2_{KK}$ expression as the environmental conditions stifle $\alpha1_{NN}$ NKA transport in the salt gland due to the extreme voltage across the basolateral membrane.

Contribution of the Noncanonical Substitutions to High Salinity Adaptation. The finding that $\alpha2_{KK}$ operates with a reduced stoichiometry raises the question as to whether this isoform is needed to adapt to high salinity. When *Artemia* adapt to 4 M salinities, there is a concomitant remarkable ~800-fold increase in $\alpha2_{KK}$ mRNA. However, the $\alpha2_{KK}$ transcript increase is much more variable at 2 M salt (Fig. 1*E*), only fourfold higher salinity than normal sea water. Jorgensen and Amat (12) reported a similar increase in $\alpha2_{KK}$ mRNA at high salinity. The variable expression of $\alpha2_{KK}$ that we observed at 2 M may indicate that at Na^+ gradients around 2 M salt, the electrochemical potential may become too steep for canonical NKAs thus setting up the need for $\alpha2_{KK}$ pumps. If α_{2KK} pumps were apically localized, their function would be more straightforward to understand, i.e., pumping Na^+ back into the environment (or gut lumen). However, the concentration of mitochondria toward the basolateral membrane (37) suggests that increased $\alpha2_{KK}$ expression occurs on the basolateral side. Thus, salt extrusion in *Artemia* salt glands probably follows the model proposed by Conte (3), where Na^+ is extruded through the paracellular pathway and Cl^- is extruded across the cell, using the Na^+,K^+,2Cl^--cotransporter (NKCC) powered by the basolateral Na^+ gradient and an apical Cl^- channel, a candidate being the newly described CFTR homologue (38). Passive apical Cl^- extrusion requires a very negative voltage that must be generated by the NKA.

Hemolymph bathing the basolateral membrane contains 125 mM Na^+ and 6 mM K^+ (1). A back of the envelope calculation assuming the intracellular Na^+ concentration in salt glands and gut cells is 10–20 mM, as in most cells from osmoregulating animals, puts the equilibrium potential for Na^+ (given by the Nernst equation, $E_{Na} = -\frac{RT}{F}\ln\{\frac{[Na]i}{[Na]o}\}$, where R is the gas constant, T the absolute temperature and F the Faraday constant) at ~+60 mV at 25 °C. Consequently, the 500–600 mV of energy available from hydrolysis of one ATP molecule (36) would be insufficient to support simultaneous transport of 3 Na^+ ions if the basolateral voltage is more negative than ~−90 mV, in which case translocating 3 Na^+ would cost 450 mV (150 mV per Na^+) plus enthalpy (heat generation). Estimates of NKA efficiency indicate that under physiological conditions, ~15% of the free energy from ATP hydrolysis is released as heat (39), bringing the cost to ~520 mV, the maximal available energy. However, the energy from ATP hydrolysis at −90 mV is enough to transport 2 Na^+ per ATP hydrolyzed (300 mV plus enthalpy). Although the trans-basolateral voltage has never been measured in these epithelia, Conte (40) reported the Na^+ dependence of the transepithelial voltage as +75 mV, at 2.5 M external NaCl, slightly below the equilibrium potential for Na^+. This value would increase at higher Na^+, as the equilibrium potential for Na^+ across the epithelium is raised. If we consider the augmented expression of $\alpha2_{KK}$, it is reasonable that these pumps would contribute to generate voltages much more negative than −90 mV.

Brine shrimp and brine fly larvae (*Ephydra*) are the only animals known to dwell in the Great Salt Lake in Utah, when salinities are above 2 M. *Ephydra cinerea* are the most abundant brine fly but the most detailed study on salinity tolerance has been done in the alkali fly *Ephydra (Cirrula) hyans* (41, 42). In contrast to brine shrimp, *Ephydra* cannot tolerate salinities above 180 g/L (sodium carbonate instead of sodium chloride), corresponding to about 2 M salt. A search for NKA sequences in the published genome of *Ephydra gracilis* indicates the presence of canonical sodium pumps without noncanonical ones. The fact that the brine fly larvae are less tolerant to extreme salinities is further evidence pointing to $\alpha2_{KK}$ noncanonical pumps as essential for adaptation to salinities above ~2 M.

The genome of another branchiopod crustacean, the freshwater flea (*Daphnia*) has an $\alpha2_{KK}$ pump with lysine residues at the positions equivalent to N333 and N785. The reason for their inability to survive high salinity is unclear but is probably related to the lack of an impermeable integument. *Daphnia* living in salinities up to 8 g/L (~125 mM) increase the expression of both $\alpha1_{NN}$ and $\alpha2_{KK}$ isoforms (43). *Artemia* and *Daphnia* $\alpha2_{KK}$ pumps share 72% sequence identity. It has identical TM4, TM5 and TM6 segments, but with very dissimilar inter-transmembrane loops, including loops 1–2, 2–3, and 5–6 known to be important to determine ion affinities and occlusion (44). We hypothesize that the $\alpha2_{KK}$ pumps of freshwater branchiopods have been modified to play a role in fighting a very large gradient in the opposite direction, allowing them to absorb Na^+ from low-salinity environments. Interestingly, fishes that adapt to freshwater like cichlids (45), salmonids (46), and zebrafish (47, 48) frequently have one K785 containing α1 subisoform whose mRNA expression increases in the gills when the animals adapt to low salinity, a phenomenon thought to allow them to absorb Na^+ from freshwater via gill epithelia. Future studies will evaluate how these and other K785 containing NKAs interact with other ion-transport mechanisms to collectively enable adaptation to both high and low extreme salinity environments.

Methods

Brine Shrimp Rearing and Maintenance. *Artemia franciscana* cysts (Brine Shrimp Direct) were hatched in three tanks: one at half strength Instant Ocean™ artificial sea water (~250 mM NaCl) and two others in full strength artificial sea water supplemented with 1.5 M NaCl (~2 M NaCl) after hatching, one of the 2 M tanks was left to evaporate until it reached ~4 M salt (as assessed by osmolality). Animals were collected after more than a week under these conditions. Before animal collection, water salinity was confirmed by measuring osmolality of the solution with a Wescor osmometer. Aquariums were maintained at 26–28 °C under continuous light and aeration. Feeding the shrimp with algae began 12 h posthatching and continued once or twice daily until collection.

Transcriptome Assembly and NKA Isoform Verification. We assembled an *Artemia franciscana* transcriptome from RNASeq data to determine the number of NKA isoforms present and their sequences. To capture sufficient RNA for library preparation, 5–10 whole individuals were pooled together in each sample and RNA was extracted using Trizol. The transcriptome was assembled from three samples at 250 mM, three samples at 2 M, and two samples at 4 M treatments, each with 2 × 150 bp Illumina sequencing. To minimize the unnecessary addition of read errors, each sample was truncated to 40 million reads, as suggested by MacManes (49). Reads were cleaned with trimmomatic (50), filtered through khmer (51) without digital normalization, and input to Trinity (52). This workflow was facilitated by the elvers pipeline (53). Transcriptome assembly statistics are shown in *SI Appendix*, Table S1.

Prospective α and β subunit isoforms of NKA were found within the transcriptome by BLAST searches (54) with known *Artemia* sequences. To verify the nucleotide sequences of each hit, fastp-processed reads from one sample were aligned with bowtie2 (55) using local alignments with an ambiguous base penalty of

zero to the prospective subunit isoforms. Mapped reads were then sorted with samtools (56) and visualized using IGV (57). When discrepancies existed between transcriptome sequences and the mapped reads, the transcriptome sequences were altered to match the reads. This process was conducted iteratively until the sequences had full continuous support by read mapping. Each sequence was then confirmed by Sanger sequencing. SNPs that resulted in differing amino acid sequences were verified in both NGS and Sanger sequencing.

Real-Time Quantitative PCR. Quantitative real-time PCR was performed using the Applied Biosystems PowerSYBR™ Green PCR system (Fisher Scientific, #4368702) as per the manufacturer's recommended protocol. Briefly, the PCR reactions (1x *Power*SYBR™ Green PCR Master Mix, 300 nM forward primer, 300 nM reverse primer, and 0.5 μg template cDNA) were aliquoted into a MicroAmp® EnduraPlate™ Optical 96-Well reaction plate in triplicate. These reactions were performed using Applied Biosystems Quant Studio 3 Real Time PCR System under the following conditions: A hold stage consisting of 2 min at 50 °C, 10 min at 95 °C; a PCR stage consisting of 40 cycles of 95 °C for 15 s and 60 °C or 30 s; and a melt curve stage consisting of 95 °C for 15 s followed by cooling to 60 °C for 1 min before ramping to 95 °C at 0.1 °C/s.

Primers for qPCR were designed to target specific amplification of the α and β isoforms as well as control housekeeping genes (*SI Appendix*, Table S2). Primer specificity was determined visualizing single product bands of anticipated size via agarose gel electrophoresis (2%). Primer efficiency was determined by performing the qPCR reaction with decreasing concentration of template cDNA following a 5x serial dilution scheme and finding the slope of the resultant standard curve of Ct values vs. log(cDNA copy #).

Expression and Purification of $\alpha2_{KK}\beta2$ for Cryo-EM. Procedures for protein expression and purification are essentially the same as those reported previously (33, 58). Briefly, a hexa-histidine tag and the enhanced green fluorescence protein (EGFP) were inserted in the amino-terminal side of Leu16 of the brine shrimp $\alpha2_{KK}$ subunit and followed by a tobacco etch virus (TEV) protease recognition sequence and subcloned into a hand-made vector. The wildtype brine shrimp β2-subunit was also cloned with the Flag epitope tag (DYKDDDDK) and the TEV protease recognition site in its N terminus. The $\alpha2_{KK}\beta2$-complex was expressed using baculovirus-mediated transduction of mammalian HEK293S GnT1$^-$ cells [BacMam (59) purchased from ATCC. Cells were directly solubilized with 1% lauryl maltose neopentyl glycol (LMNG) in the presence of 40 mM MES/Tris (pH 6.5), 10% glycerol, 5 mM dithiothreitol, 1 mM $MgCl_2$, in the presence of 50 mM Choline-Cl, 1 mM $AlCl_3$, 4 mM NaF and 5 mM ADP (tris salt) on ice for 20 min. After removal of insoluble material by ultracentrifugation, the supernatant was mixed with anti-FLAG M2 resin (Sigma) at 4 °C for 3 h, which was followed by washing with buffer containing 40 mM MES/Tris (pH 6.5), 5% glycerol, 1 mM $MgCl_2$, and 0.06% glycerol-diosgenin (GDN), in the presence of 50 mM Choline-Cl, 1 mM $AlCl_3$, 4 mM NaF, and 0.1 mM ADP. After addition of TEV protease and endoglycosidase, anti-GFP nanobody was incubated at 4 °C overnight. Digested peptide fragments containing EGFP and endoglycosidase were removed by passing the fractions through a Ni-NTA resin (Qiagen). Flow-through fractions were concentrated and subjected to a size-exclusion column chromatograph using a Superrose6 Increase column equilibrated in buffer comprising 20 mM MES/Tris (pH 6.5), 1% glycerol, 1 mM $MgCl_2$, and 0.06% GDN with 50 mM Choline-Cl, 1 mM $AlCl_3$, 4 mM NaF, and 0.1 mM ADP. Peak fractions were collected and concentrated to 8 mg/mL. The final concentration of 5 mM ADP was added to the protein sample.

Cryo-EM. The purified protein samples (at 8 mg/mL) were applied to a freshly glow-discharged Quantifoil holey carbon grid (R1.2/1.3, Cu/Rh, 300 mesh), using a Vitrobot Mark IV (FEI) at 4 °C with a blotting time of 4 s under 99% humidity, and the grids were then plunge-frozen in liquid ethane. Prepared grids were transferred to a CRYO ARM 300 microscope (JEOL), running at 300 kV and equipped with a Gatan K3 Summit direct electron detector in the electron counting mode. Imaging was performed at a nominal magnification of 60,000×, corresponding to a calibrated pixel size of 0.753 Å/pix (SPring-8 EM01CT). Each movie was recorded in a correlated-double sampling (CDS) mode for 2.6 s and subdivided into 60 frames. The electron flux was set to 8.46 e^-/pix/s at the detector, resulting in an accumulated exposure of 60 $e^-/Å^2$ at the specimen. The data were automatically acquired by the image shift method using SerialEM software (60), with a defocus range of −0.8 to −1.8 μm. The dose-fractionated movies were subjected to beam-induced motion correction, using Relion 3.1 (61), and the contrast transfer function (CTF) parameters were estimated using patch CTF estimation using cryoSPARC v4 (62).

For each dataset, particles were initially picked by blob picker using cryoSPARC and extracted with down-sampling to a pixel size of 3.0 Å/pix. These particles were subjected to several rounds of 2D classifications. The 2D classes that show clear secondary structures were then subjected to ab initio reconstruction in four models, and these are further refined by heterogenous refinement. Part of 2D classes that were not used for the initial ab-initio reconstruction (i.e., second best) were subjected to ab initio reconstruction, and these apparently junk particles were subjected to the heterogenous refinement together with the best class obtained from the initial heterogenous refinement. This operation increases the number of particles reconstituted in the best class. After several rounds of iterative process, particles were subjected to nonuniform refinement. The particles were re-extracted with a pixel size of 1.35 Å/pix and subjected to heterogeneous refinement to remove junk particles. The best class is further processed by nonuniform refinement with per-particle defocus refinement, beam-tilt refinement in cryoSPARC. (The flow chart for analysis is shown in *SI Appendix*, Fig. S3*F*). The particle set was then transferred to Relion to perform Bayesian polishing (63). Polished particles were extracted with 0.752 Å/pix, reimported to cryoSPARC and performed nonuniform refinement (*SI Appendix*, Fig. S3*F*). Resolution of the analyzed map was defined according to the FCS = 0.143 criterion (64) (*SI Appendix*, Fig. S3*D*). The local resolution and angular distributions for each structure were estimated by cryoSPARC (*SI Appendix*, Fig. S3*C*). All the models were manually built in Coot 0.9.4 (65) using the homology model derived from the crystal structure of NKA in (K^+)E2-P state (2zxe). Phenix (66) was used for refinement of other regions. Correlations between build model and EM maps (full, half) are also shown in *SI Appendix*, Fig. S3*E*. The model contained 93.76/6.24/0.0% in the favored, allowed, and outlier regions of the Ramachandran plot, respectively.

Oocyte Isolation and Molecular Biology. Oocytes were isolated from anesthetized female *Xenopus laevis* frogs, as previously described (67), and kept until the day of recording in S.O.S. solution (in mM: 100 NaCl, 2 KCl, 1.8 $CaCl_2$, 1 $MgCl_2$, and 5 HEPES, pH 7.4) supplemented with horse serum and antimycotic-antibiotic solution (Anti-Anti, Gibco) at 16 °C. All procedures were done in accordance with the institutional animal care and use committee. Codon-optimized version of *Artemia*'s $\alpha2_{KK}$ (accession number P17326), β1 and β2 were cloned into the pSD5 vector by Gibson assembly. The *Xenopus* α1 ouabain-resistant Q120RN131D-*Xenopus* α1-subunit was used as a template for mutations mimicking $\alpha2_{KK}$. For simplicity, we refer to this so-called "RD" template as wild type. Plasmid cDNA was linearized using BglII (New England BioLabs) and cRNA was transcribed using SP6 mMessage machine (Ambion). The cRNAs encoding α subunits (50 ng) were mixed in equimolar ratios with a β subunit (*Xenopus* α1β3 and *Artemia* α2β1 or α2β2) and injected into healthy oocytes 3-d before recording.

Recording Solutions. For TEVC, extracellular solutions contained (in mM): 133 methanesulfonic acid (MS), 5 $Ba(OH)_2$, 1 $Mg(OH)_2$, 0.5 $Ca(OH)_2$, and 10 HEPES, with 125 N-methyl D-glucamine (NMG^+) or 125 NaOH to pH 7.6. K^+ was added to extracellular solutions from a 450 mM K-MS stock. For ^{86}Rb uptake experiments, the extracellular solutions contained (in mM): 120 NMG^+, 5 $Ba(OH)_2$, 1 $Mg(OH)_2$, 0.5 $Ca(OH)_2$, 10 HEPES and 0.05 bumetanide to inhibit the NKCC (pH 7.6 with HCl). RbCl was added to extracellular NMG^+ from a 200 mM RbCl stock, to which $^{86}RbCl$ was added. For patch-clamp experiments, the patch was formed in a solution containing (in mM): 100 aspartic acid, 100 KOH, 20 KCl, 10 HEPES, 4 $MgCl_2$, and 2 EGTA, pH 7.0. Immediately after excision, the bath solution was switched to the experimental intracellular solutions composed of 1 $MgCl_2$, 10 Tetraethylammonium (TEA)-Cl, 5 EGTA, 10 HEPES, and 110 glutamic acid, with either 125 NMG^+ or 125 NaOH, pH 7.4. Intermediate intracellular Na^+ concentrations were obtained mixing NMG^+ and Na^+ solutions. MgATP was added from 200 mM stocks (pH 7.4 with NMG^+). The extracellular pipette solution contained 1 μM ouabain to inhibit endogenous pumps and (in mM) 125 NMG, 5 $BaCl_2$, 1 $MgCl_2$, 0.5 $CaCl_2$, 10 HEPES, and 5 mM KCl (pH 7.4 with HCl) to measure NKA current.

Electrophysiology. TEVC was performed as previously described (27). Before recording, oocytes were Na^+-loaded by ≥1-h incubation in a solution containing (in mM): 90 Na-sulfamate, 20 HEPES, 20 TEA-Cl, and 0.2 EGTA (pH 7.2 with NaOH), supplemented with 2-10 μM ouabain to inhibit endogenous pumps.

In $^{86}Rb^+$ uptake experiments, after withdrawal of $^{86}Rb^+$ from the NMG^+ bath solution oocytes were individually placed in a scintillation tube with 3 mL of ScintiVerse BD (Thermo-Fisher Scientific) and radioactivity determined by liquid scintillation spectroscopy (LS6500 liquid scintillation Counter, Beckman-Coulter). The average uptake in uninjected oocytes under TEVC (i.e., the non-NKA-mediated uptake) was subtracted from the uptake in each injected oocyte before dividing by the extruded charge to obtain the stoichiometry in individual oocytes. Inside-out patches were performed as described (67).

Data Analysis. Electrophysiological data were analyzed using pClamp and Origin (OriginLab Corp.). $K_{0.5}$ values for extracellular K^+ or intracellular Na^+ were obtained by fitting the Hill equation:

$$I = I_{max}\left([S]^{nH} / \left(K_{0.5}^{nH} + [S]^{nH} \right) \right),$$

to the steady-state ion-induced currents at each voltage as a function of ion concentration, where I_{max} is the maximal current activated at a saturating concentration of the ion (S), n_H is the Hill coefficient, and $K_{0.5}$ the concentration inducing half-maximal current activation.

The transient currents elicited by voltage pulses from −50 mV to different voltages were integrated and the charge moved was plotted against the applied voltage to obtain the "Q-V" curves. A Boltzmann distribution was fitted to the Q-V data (27):

$$Q = Q_{hyp} - Q_{tot} / \left(1 + \exp\left(z_q e \left(V - V_{1/2}\right) / kT\right)\right),$$

where Q_{hyp} is the charge moved by hyperpolarizing voltage pulses, Q_{tot} is the total charge moved, and $V_{1/2}$ is the midpoint voltage; e is the elementary charge, k is the Boltzmann constant, T is the absolute temperature, and z_q is the apparent valence of a charge crossing the whole electric field. kT/ez_q is the slope factor. The data in Fig. 3*D* are presented normalized (by subtracting Q_{hyp} and dividing by Q_{tot}) to highlight the change in $V_{1/2}$ usually associated with changes in extracellular Na^+ apparent affinity (27).

Simulations. MD simulations of canonical NKAs with the mutations N333K, N785K, or N333K/N785K ($\alpha1_{K333}$, $\alpha1_{K785}$, and $\alpha1_{KK}$, respectively) were carried out as previously described for the wild-type pump (23). Briefly, the crystal structures 3WGV (13) and 2ZXE (14) representing the transition-state phosphate analogue-inhibited conformation E1.ADP.Pi with $3Na^+$ ions bound and E2.Pi with 2 K^+ ions bound, respectively, were used in the corresponding simulations of the pump embedded in a POPC membrane bilayer. In 3WGV, chains A (α-subunit), B (β-subunit), and G (γ-subunit) were kept. For each condition, three copies of the system were simulated. The most favorable rotameric states of the lysine substitutions were determined by scanning the side chain torsion angles (χ_{1-4}) and calculating the energy of the entire system. The 10 lowest energy systems were recorded. Three systems from the 10, including the one with the lowest energy, were simulated. Four additional sets of simulations with the bound ions (Na^+ or K^+) removed from either site I or site II were included for the $\alpha1_{KK}$ double mutant in both E1 and E2 structural models. Before the simulations started, the protonation state of the binding-site residues was assigned using PROPKA3.1 (68). Each system was subjected to a 675-ps equilibration with reducing restraints on the nonhydrogen atoms to relax the initially uncorrelated components, followed by a 10-ns unrestrained preproduction using the simulation package NAMD2.11 (69). After equilibration, the systems were simulated for hundreds of ns each using the special-purpose supercomputer Anton (70), which is designed for long time scale simulations (Table 1).

Data, Materials, and Software Availability. All study data are included in the article and/or *SI Appendix*. The full structural data can be accessed PDB (8K1L) (71) and EMDB (EMD-36794) (72) and the assembled transcriptome has been deposited in NCBI (BioProject PRJNA1043900) (73).

ACKNOWLEDGMENTS. This work was supported by grants from NSF (MCB-2003251) to P.A and C.G. and (MCB-2309048) to B.R. M.A.B. was supported by an NSF Postdoctoral Research Fellowship in Biology (DBI-1907197). K.A. was supported by a Grant-in-Aid for Scientific Research (21H02426) and the Daiichi Sankyo Foundation of Life Science, JST CREST Grant Number JPMJCR22E4 to K.A. We thank Dr. Michael C. Wiener for comments on the manuscript, Dr. Josh J Rosenthal at the MBL for advice on transcriptome analysis, and Drs. A. Oshima, K. Tanaka, G. Christoph, C.C. Gopalasingam, and H. Shigematsu for cryo-EM analysis.

Author affiliations: [a]Department of Cell Physiology and Molecular Biophysics, Center for Membrane Protein Research, Texas Tech University Health Sciences Center, Lubbock, TX 79430; [b]School of Biological Sciences, Illinois State University, Normal, IL 61790; [c]Department of Biochemistry and Molecular Biology, The University of Chicago, Chicago, IL 60637; [d]Department of Biology, Saint Francis University, Loretto, PA 15940; and [e]Department of Basic Medical Sciences, Cellular and Structural Physiology Institute, Graduate School of Pharmaceutical Sciences, Nagoya University, Nagoya 464-8601, Japan

1. D. Russler, J. Mangos, Micropuncture studies of the osmoregulation in the nauplius of *Artemia salina*. *Am. J. Physiol.* **234**, R216–R222 (1978).
2. C. W. Holliday, D. B. Roye, R. D. Roer, Salinity-induced changes in branchial Na+/K+-ATPase activity and transepithelial potential difference in the brine shrimp *Artemia sauna*. *J. Exp. Biol.* **151**, 279–296 (1990).
3. F. P. Conte, Molecular domains in epithelial salt cell NaCl of crustacean salt gland (*Artemia*). *Int. Rev. Cell Mol. Biol.* **268**, 39–57 (2008).
4. F. P. Conte, S. R. Hootman, P. J. Harris, Neck organ of *Artemia salina* nauplii. *J. Comp. Physiol.* **80**, 239–246 (1972).
5. E. Copeland, Salt transport organelle in *Artemia salenis* (brine shrimp). *Science (New York, N.Y.)* **151**, 470–471 (1966).
6. C. Gatto, S. M. McLoud, J. H. Kaplan, Heterologous expression of Na(+)-K(+)-ATPase in insect cells: Intracellular distribution of pump subunits *Am. J. Physiol. Cell Physiol.* **281**, C982–992 (2001).
7. C. M. Stanley *et al.*, Importance of the voltage dependence of cardiac Na/K ATPase isozymes. *Biophys. J.* **109**, 1852–1862 (2015).
8. G. Blanco, Na, K-ATPase subunit heterogeneity as a mechanism for tissue-specific ion regulation. *Semin. Nephrol.* **25**, 292–303 (2005).
9. A. K. Sen, R. L. Post, Stoichiometry and localization of adenosine triphosphate-dependent sodium and potassium transport in the erythrocyte. *J. Biol. Chem.* **239**, 345–352 (1964).
10. G. L. Peterson, L. E. Hokin, Improved purification of brine-shrimp (*Artemia saline*) (Na+ + K+)-activated adenosine triphosphatase and amino-acid and carbohydrate analyses of the isolated subunits *Biochem. J.* **192**, 107–118 (1980).
11. L. A. Baxter-Lowe, J. Z. Guo, E. E. Bergstrom, L. E. Hokin, Molecular cloning of the Na, K-ATPase alpha-subunit in developing brine shrimp and sequence comparison with higher organisms. *FEBS Lett.* **257**, 181–187 (1989).
12. P. L. Jorgensen, F. Amat, Regulation and function of lysine-substituted Na, K pumps in salt adaptation of *Artemia franciscana*. *J. Membrane Biol.* **221**, 39–49 (2008).
13. R. Kanai, H. Ogawa, B. Vilsen, F. Cornelius, C. Toyoshima, Crystal structure of a Na+-bound Na+, K+-ATPase preceding the E1P state *Nature* **502**, 201–206 (2013).
14. T. Shinoda, H. Ogawa, F. Cornelius, C. Toyoshima, Crystal structure of the sodium-potassium pump at 2.4 A resolution. *Nature* **459**, 446–450 (2009).
15. K. K. Bhattacharyya, E. E. Bergstrom, L. E. Hokin, Molecular cloning of the beta-subunit of the Na, K-ATPase in the brine shrimp, *Artemia*. The cDNA-derived amino acid sequence shows low homology with the beta-subunits of vertebrates except in the single transmembrane and the carboxy-terminal domains. *FEBS Lett.* **269**, 233–238 (1990).
16. M. T. Macias, I. Palmero, L. Sastre, Cloning of a cDNA encoding an *Artemia franciscana* Na/K ATPase alpha-subunit. *Gene* **105**, 197–204 (1991).
17. S. De Vos *et al.*, The genome of the extremophile *Artemia* provides insight into strategies to cope with extreme environments. *BMC Genomics* **22**, 635 (2021).
18. D. J. Meyer *et al.*, FXYD protein isoforms differentially modulate human Na/K pump function. *J. General Physiol.* **152**, e202012660 (2020).
19. J. D. Horisberger, S. Kharoubi-Hess, Functional differences between alpha subunit isoforms of the rat Na, K-ATPase expressed in *Xenopus* oocytes. *J. Physiol.* **539**, 669–680 (2002).
20. N. N. Tavraz *et al.*, Diverse functional consequences of mutations in the Na+/K+-ATPase alpha2-subunit causing familial hemiplegic migraine type 2. *J. Biol. Chem.* **283**, 31097–31106 (2008).
21. C. Colina *et al.*, Structural basis of Na(+)/K(+)-ATPase adaptation to marine environments. *Nat. Struct. Mol. Biol.* **14**, 427–431 (2007).
22. K. S. Stanley, V. C. Young, C. Gatto, P. Artigas, External ion access in the Na/K pump: Kinetics of Na(+), K(+), and quaternary amine interaction. *Biophys. J.* **115**, 361–374 (2018).
23. H. Rui, P. Artigas, B. Roux, The selectivity of the Na(+)/K(+)-pump is controlled by binding site protonation and self-correcting occlusion. *eLife* **5**, e16616 (2016).
24. A. Sagar, R. F. Rakowski, Access channel model for the voltage dependence of the forward-running Na+/K+ pump *J. Gen. Physiol.* **103**, 869–893 (1994).
25. F. Bezanilla, C. A. Villalba-Galea, The gating charge should not be estimated by fitting a two-state model to a Q-V curve. *J. Gen. Physiol.* **142**, 575–578 (2013).
26. M. Holmgren, R. F. Rakowski, Charge translocation by the Na+/K+ pump under Na+/Na+ exchange conditions: Intracellular Na+ dependence *Biophys. J.* **90**, 1607–1616 (2006).
27. K. Spontarelli *et al.*, Role of a conserved ion-binding site tyrosine in ion selectivity of the Na+/K+ pump. *J. Gen. Physiol.* **154**, e202113039 (2022).
28. C. Hegyvary, R. L. Post, Binding of adenosine triphosphate to sodium and potassium ion-stimulated adenosine triphosphatase. *J. Biol. Chem.* **246**, 5234–5240 (1971).
29. K. Abe, K. Yamamoto, K. Irie, T. Nishizawa, A. Oshima, Gastric proton pump with two occluded K(+) engineered with sodium pump-mimetic mutations *Nat. Commun.* **12**, 5709 (2021).
30. H. N. Nielsen *et al.*, Distinct effects of Q925 mutation on intracellular and extracellular Na(+) and K(+) binding to the Na(+), K(+)-ATPase. *Sci. Rep.* **9**, 13344 (2019).
31. A. P. Einholm, M. S. Toustrup-Jensen, R. Holm, J. P. Andersen, B. Vilsen, The rapid-onset dystonia parkinsonism mutation D923N of the Na+, K+-ATPase alpha3 isoform disrupts Na+ interaction at the third Na+ site *J. Biol. Chem.* **285**, 26245–26254 (2010).
32. H. Poulsen *et al.*, Neurological disease mutations compromise a C-terminal ion pathway in the Na(+)/K(+)-ATPase. *Nature* **467**, 99–102 (2010).

33. V. C. Young *et al.*, Structure and function of H+/K+ pump mutants reveal Na+/K+ pump mechanisms. *Nat. Commun.* **13**, 5270 (2022).
34. R. Holm *et al.*, Arginine substitution of a cysteine in transmembrane helix M8 converts Na+, K+-ATPase to an electroneutral pump similar to H+, K+-ATPase. *Proc. Natl. Acad. Sci. U.S.A.* **114**, 316–321 (2017).
35. M. Burnay, G. Crambert, S. Kharoubi-Hess, K. Geering, J. D. Horisberger, Electrogenicity of Na, K- and H, K-ATPase activity and presence of a positively charged amino acid in the fifth transmembrane segment. *J. Biol. Chem.* **278**, 19237–19244 (2003).
36. P. De Weer, D. C. Gadsby, R. F. Rakowski, Voltage dependence of the Na-K pump. *Annu. Rev. Physiol.* **50**, 225–241 (1988).
37. R. J. Lowy, F. P. Conte, Morphology of isolated crustacean larval salt glands. *Am. J. Physiol.* **248**, R709–716 (1985).
38. A. Q. Li *et al.*, The chloride channel cystic fibrosis transmembrane conductance regulator (CFTR) controls cellular quiescence by hyperpolarizing the cell membrane during diapause in the crustacean *Artemia*. *J. Biol. Chem.* **294**, 6598–6611 (2019).
39. R. Noske, F. Cornelius, R. J. Clarke, Investigation of the enzymatic activity of the Na+, K+-ATPase via isothermal titration microcalorimetry. *Biochim. Biophys. Acta* **1797**, 1540–1545 (2010).
40. F. P. Conte, Structure and function of the crustacean larval salt gland. *Intern. Rev. Cytol.* **91**, 45–106 (1984).
41. D. B. Herbst, Developmental and reproductive costs of osmoregulation to an aquatic insect that is a key food resource to shorebirds at salt lakes threatened by rising salinity and desiccation. *Front. Ecol. Evol.* **11**, 1136966 (2023).
42. D. B. Herbst, F. P. Conte, V. J. Brookes, Osmoregulation in an alkaline salt lake insect, *Ephydra* (*Hydropyrus*) *hians* Say (Diptera: Ephydridae) in relation to water chemistry. *J. Insect Physiol.* **34**, 903–909 (1988).
43. L. C. Latta, L. J. Weider, J. K. Colbourne, M. E. Pfrender, The evolution of salinity tolerance in Daphnia: A functional genomics approach. *Ecol. Lett.* **15**, 794–802 (2012).
44. C. Colina, J. P. Palavicini, D. Srikumar, M. Holmgren, J. J. Rosenthal, Regulation of Na+/K+ ATPase transport velocity by RNA editing *PLoS Biol.* **8**, e1000540 (2010).
45. C. K. Tipsmark *et al.*, Switching of Na+, K+-ATPase isoforms by salinity and prolactin in the gill of a cichlid fish. *J. Endocrinol.* **209**, 237–244 (2011).
46. P. L. Jorgensen, Importance for absorption of Na+ from freshwater of lysine, valine and serine substitutions in the alpha1a-isoform of Na, K-ATPase in the gills of rainbow trout (*Oncorhynchus mykiss*) and Atlantic salmon (*Salmo salar*). *J. Membrane Biol.* **223**, 37–47 (2008).
47. A. J. Esbaugh, K. V. Brix, M. Grosell, Na(+) K(+) ATPase isoform switching in zebrafish during transition to dilute freshwater habitats *Proc. Biol. Sci.* **286**, 20190630 (2019).
48. B. K. Liao, R. D. Chen, P. P. Hwang, Expression regulation of Na+-K+-ATPase alpha1-subunit subtypes in zebrafish gill ionocytes *Am. J. Physiol. Regul. Integr. Comp. Physiol.* **296**, R1897–R1906 (2009).
49. M. D. MacManes, Establishing evidenced-based best practice for the de novo assembly and evaluation of transcriptomes from non-model organisms. bioRxiv [Preprint] (2016). https://doi.org/10.1101/035642 (Accessed 10 February 2020).
50. A. M. Bolger, M. Lohse, B. Usadel, Trimmomatic: A flexible trimmer for Illumina sequence data. *Bioinformatics (Oxford, England)* **30**, 2114–2120 (2014).
51. M. R. Crusoe *et al.*, The khmer software package: Enabling efficient nucleotide sequence analysis. *F1000Research* **4**, 900 (2015).
52. M. G. Grabherr *et al.*, Full-length transcriptome assembly from RNA-Seq data without a reference genome. *Nat. Biotechnol.* **29**, 644–652 (2011).
53. N. T. Pierce, L. K. Johnson, C. T. Brown, C. Reid, K. Leinweber, dib-lab/elvers: v0.1. Github. https://github.com/dib-lab/elvers. Accessed 15 April 2019.
54. C. Camacho *et al.*, BLAST+: Architecture and applications. *BMC Bioinf.* **10**, 421 (2009).
55. B. Langmead, S. L. Salzberg, Fast gapped-read alignment with Bowtie 2. *Nat. Methods* **9**, 357–359 (2012).
56. H. Li *et al.*, The sequence alignment/map format and SAMtools. *Bioinformatics (Oxford, England)* **25**, 2078–2079 (2009).
57. H. Thorvaldsdóttir, J. T. Robinson, J. P. Mesirov, Integrative Genomics Viewer (IGV): high-performance genomics data visualization and exploration. *Brief. Bioinf.* **14**, 178–192 (2013).
58. K. Abe, K. Irie, H. Nakanishi, H. Suzuki, Y. Fujiyoshi, Crystal structures of the gastric proton pump. *Nature* **556**, 214–218 (2018).
59. A. Dukkipati, H. H. Park, D. Waghray, S. Fischer, K. C. Garcia, BacMam system for high-level expression of recombinant soluble and membrane glycoproteins for structural studies. *Protein Expr. Purif.* **62**, 160–170 (2008).
60. D. N. Mastronarde, Automated electron microscope tomography using robust prediction of specimen movements. *J. Struct. Biol.* **152**, 36–51 (2005).
61. J. Zivanov *et al.*, New tools for automated high-resolution cryo-EM structure determination in RELION-3. *eLife* **7**, e42166 (2018).
62. A. Punjani, J. L. Rubinstein, D. J. Fleet, M. A. Brubaker, cryoSPARC: Algorithms for rapid unsupervised cryo-EM structure determination. *Nat. Methods* **14**, 290–296 (2017).
63. J. Zivanov, T. Nakane, S. H. W. Scheres, A Bayesian approach to beam-induced motion correction in cryo-EM single-particle analysis. *IUCrJ* **6**, 5–17 (2019).
64. P. B. Rosenthal, R. Henderson, Optimal determination of particle orientation, absolute hand, and contrast loss in single-particle electron cryomicroscopy. *J. Mol. Biol.* **333**, 721–745 (2003).
65. P. Emsley, K. Cowtan, Coot: Model-building tools for molecular graphics. *Acta Crystallogr. D, Biol. Crystallogr.* **60**, 2126–2132 (2004).
66. P. D. Adams *et al.*, PHENIX: A comprehensive Python-based system for macromolecular structure solution. *Acta Crystallogr. D, Biol. Crystallogr.* **66**, 213–221 (2010).
67. K. S. Stanley, D. J. Meyer, C. Gatto, P. Artigas, Intracellular requirements for passive proton transport through the Na(+), K(+)-ATPase. *Biophys. J.* **111**, 2430–2439 (2016).
68. M. H. M. Olsson, C. R. Sondergaard, M. Rostkowski, J. H. Jensen, PROPKA3: Consistent treatment of internal and surface residues in empirical pK(a) predictions. *J. Chem. Theory Comput.* **7**, 525–537 (2011).
69. J. C. Phillips *et al.*, Scalable molecular dynamics with NAMD. *J. Comput. Chem.* **26**, 1781–1802 (2005).
70. D. E. Shaw *et al.*, "Millisecond-scale molecular dynamics simulations on Anton" in *Proceedings of the Conference on High Performance Computing Networking, Storage and Analysis* (ACM, 2009), p. 39.
71. K. Abe, P. Artigas, Cryo-EM structure of Na^+, K^+-ATPase alpha2 from *Artemia salina* in cation-free E2P form. Protein Data Bank. https://doi.org/10.2210/pdb8K1L/pdb. Deposited 10 July 2023.
72. K. Abe, P. Artigas, Cryo-EM structure of Na^+, K^+-ATPase alpha2 from *Artemia salina* in cation-free E2P form. Electron Microscopy Data Bank. https://www.ebi.ac.uk/pdbe/entry/emdb/EMD-36794. Deposited 10 July 2023.
73. M. A. Birk, V. C. Young, P. Artigas, *Artemia franciscana* transcriptome assembly. NCBI BioProject. https://www.ncbi.nlm.nih.gov/bioproject/1043900. Deposited 22 Nov 2023.